Original Article | Open Access

Legal Medicine Research

Suo *et al. Leg Med Res.* 2026;1:2 **DOI:**10.20517/lmr.2026.04

Integrating dual-transcriptomic and machine learning to establish a miRNA-mRNA-protein triad system for skin wound age estimation

Longlong Suo[1,2,#], Haomiao Yuan[1,2,3,#], Yanyan Fan[4,#], Mingzhe Wu[1,2], Shukui Du[1,2], Shuyang Mu[1,2], Jinnong Yang[1,2], Jingkai Sun[1,2], Fuyuan Zhang[1,2], Linlin Wang[1,2], Rui Zhao[1,2,5], Dawei Guan[1,2,4]

Keywords:
miRNA-mRNA-Protein, wound age estimation, forensic pathology, machine learning

Citation: Suo L, Yuan H, Fan Y, Wu M, Du S, Mu S, Yang J, Sun J, Zhang F, Wang L, Zhao R, Guan D. Integrating dual-transcriptomic and machine learning to establish a miRNA-mRNA-protein triad system for skin wound age estimation. *Leg Med Res.* 2026;1:2. https://dx.doi.org/10.20517/lmr.2026.04

Received: 1 Apr 2026
First Decision: 9 May 2026
Revised: 14 May 2026
Accepted: 26 May 2026
Published: 10 Jun 2026

Academic Editor: Teng Chen
Copy Editor: Shu-Yuan Duan
Production Editor: Shu-Yuan Duan

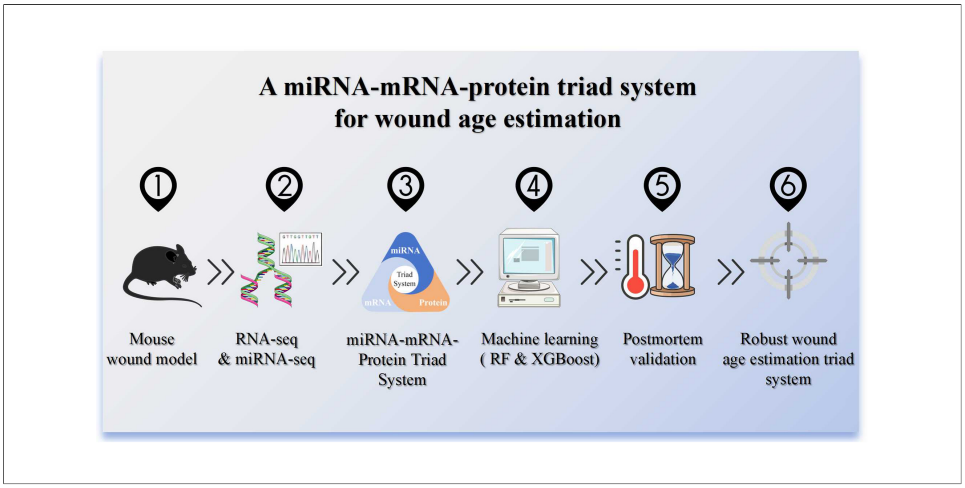

Abstract

Aim: To develop a novel miRNA-mRNA-protein triad system combined with machine learning for accurate and postmortem-robust skin wound age estimation.

Methods: Using a murine incised wound model and next-generation sequencing, we identified differentially expressed miRNAs and mRNAs during wound healing. Three triads (mmu-miR-15b-5p/*Rsad2*/RSAD2, mmu-miR-31-5p/*Cst6*/CST6, mmu-miR-1983/*Krt77*/KRT77) were established and validated. Multivariate linear regression, Random Forest, and XGBoost models were compared, and predictive performance was evaluated under different postmortem intervals (PMI).

Results: The optimal algorithm varied across triads; XGBoost generally performed best. The mmu-miR-31-5p/*Cst6*/CST6 triad maintained high accuracy ($R^2 > 0.92$) even at 4.5 d PMI,

[1]Department of Forensic Pathology, China Medical University School of Forensic Medicine, Shenyang 110122, Liaoning, China.
[2]Liaoning Province Key Laboratory of Forensic Bio-evidence Science, Shenyang 110122, Liaoning, China.
[3]Department of Emergency Medicine, Shengjing Hospital of China Medical University, Shenyang 110004, Liaoning, China.
[4]Department of Forensic Medicine, Wenzhou Medical University School of Basic Medical Sciences, Wenzhou 325035, Zhejiang, China.
[5]China Key Laboratory of Environmental Stress and Chronic Disease Control & Prevention, Ministry of Education, China Medical University, Shenyang 110122, Liaoning, China.
[#]These authors have contributed equally to the work.

Correspondence to: Dr. Linlin Wang, Dr. Rui Zhao, Dr. Dawei Guan, Department of Forensic Pathology, China Medical University School of Forensic Medicine, Shenyang 110122, Liaoning, China. E-mail: wangll@cmu.edu.cn; rzhao@cmu.edu.cn; dwguan@cmu.edu.cn

whereas the other two triads degraded faster.

Conclusion: This framework integrates a functionally validated triad with algorithm-specific modeling, enhancing wound age estimation accuracy and postmortem robustness.

INTRODUCTION

The skin is the largest organ of the human body, serving as a primary barrier against external stimuli and injuries[1]. Due to its exposed location, cutaneous wounds are among the most common types of injuries encountered in forensic practice[2]. Moreover, since skin trauma often coincides with damage to internal organs, accurately estimating the age since injury is essential not only for reconstructing events but also for inferring the age of the visceral organ trauma[3]. Therefore, skin wound age estimation has long been a major focus of forensic research worldwide[4-7].

Current methods for wound age estimation primarily fall into two categories: histological evaluation based on temporal changes during wound healing, typically divided into inflammatory, proliferative, and remodeling phases[8-10], and molecular approaches relying on time-dependent biomarkers such as cytokines, chemokines, and extracellular components[11-14]. While these markers show promise, their practical application remains limited. Postmortem degradation caused by autolysis and putrefaction significantly affects biomolecule integrity, particularly for proteins and mRNAs[15,16]. Furthermore, most studies have focused on separate, not mechanically linked biomarkers, leading to low capacity and limited accuracy for wound age determination[6,17,18].

Recent studies have highlighted the potential of miRNAs in forensic applications due to their remarkable stability, resistance to degradation, and critical regulatory roles in wound healing[19-23]. These small non-coding RNAs modulate the expression of numerous target genes, influencing various phases of skin repair[24]. However, comprehensive profiles of miRNA-mRNA regulatory networks during wound healing remain poorly characterized. In our earlier work, we identified a set of highly stable miRNA reference genes (miR-26a/30d/152) suitable for normalizing miRNA expression in the fresh wounded skin samples or those with early postmortem changes, providing a reliable foundation for subsequent quantitative analyses[25].

Building on our previous work, we further identified differentially expressed miRNAs and mRNAs in a murine model of incised skin wounds using next-generation sequencing[25]. Through integrated bioinformatic prediction and experimental validation, we established a three-dimensional biomarker panel encompassing miRNAs, their cognate target mRNAs, and the corresponding encoded proteins. Such functionally linked multi-layer integration is expected to provide more robust and accurate estimates than single-molecule approaches. To robustly model the complex multifactorial dynamics of wound healing, we deployed machine learning approaches including Random Forest (RF) and XGBoost, which excel at deconvolving latent patterns in high-dimensional datasets, enabling identification of optimal modeling strategies tailored to the intrinsic dynamics of each biomarker triad. Moreover, we systematically evaluated the impact of postmortem changes on the predictive performance of this system, addressing a critical practical concern in forensic casework.

This study establishes a novel, integrated framework for wound age estimation that combines multi-level molecular biomarkers with computational modeling, improving accuracy and robustness against postmortem degradation.

MATERIALS AND METHODS

Skin wound model and sample collection

All animal experiments were conducted in accordance with protocols approved by the Institutional Animal Care and Use Committee of China Medical University (Approval No.: cmu2019119). Male C57BL/6J mice (7 ~ 8 weeks old, 21 ± 2 g) were acclimated for one week under standard laboratory conditions. One day before surgery, dorsal hair was removed under mild anesthesia. Full-thickness linear incisions were made aseptically along the dorsal midline under isoflurane anesthesia. Postoperatively, animals were housed individually to prevent cross-contamination and wound infection. Mice were euthanized by CO_2 overdose at 12 h, 3 d, 7 d, and 14 days post-injury. Periwound skin tissue (2.0 cm × 1.0 cm) was excised and collected. Normal control mice underwent anesthesia and euthanasia under identical conditions without wound induction, and dorsal skin samples were similarly harvested. All tissue samples were immediately snap-frozen in liquid nitrogen and stored at -80 °C until further use.

RNA extraction and quality control

Total RNA was extracted from skin tissues using TRIzol reagent (#15596018CN, Invitrogen). Briefly, tissues were homogenized in TRIzol with steel beads using a high-throughput grinder (40 Hz, 30 s, 6 ~ 8 cycles). After chloroform separation and isopropanol precipitation, RNA pellets were washed with 75% ethanol, air-dried, and dissolved in DEPC-treated water. RNA concentration and purity were assessed using a NanoDrop One spectrophotometer, and integrity was evaluated with an Agilent 2100 Bioanalyzer. Samples with concentrations of 250-500 ng/μL, A_{260}/A_{280} ratios of 1.8-2.0, $A_{260}/A_{230} > 1.8$, and RNA integrity number > 7.0 were used for subsequent library construction and sequencing.

Sequencing and bioinformatic analysis

Sequencing libraries were constructed and subjected to high-throughput sequencing on an Illumina HiSeq platform. miRNA and mRNA expression levels were normalized using Transcripts Per Million and Fragments Per Kilobase of transcript per Million mapped reads, respectively. Principal component analysis (PCA) was carried out with SIMCA-P to evaluate overall sample similarity and distribution. Differential expression analysis was performed by RStudio, with significance thresholds set at $|\log_2 FC \text{ (fold change)}| > 1$ and adjusted $P < 0.05$. Temporal expression patterns of miRNAs and mRNAs across wound healing stages were identified using Short Time-series Expression Miner (STEM). Functional enrichment analysis of Gene Ontology (GO) and Kyoto Encyclopedia of Genes and Genomes (KEGG) pathways was conducted through the DAVID database, considering terms with a false discovery rate (FDR) < 0.05 and containing at least two genes as significantly enriched. miRNA- mRNA interactions were predicted using TargetScan, RNAhybrid, and miRanda. Predicted target mRNAs were further intersected with differentially expressed mRNAs derived from RNA-seq. Putative regulatory pairs with a Pearson correlation coefficient (PCC) < -0.7 and $P < 0.05$ were considered statistically significant. The miRNA - mRNA regulatory network is visualized using Cytoscape.

Determination of miRNA and mRNA by reverse transcription quantitative real-time PCR

Total RNA was extracted from skin as previously described. After quality verification, 500 ng and 250 ng of total RNA were used for miRNA and mRNA reverse transcription, respectively, using the TransScript® miRNA cDNA Synthesis SuperMix (#AT351-01, TransGen) and PrimeScript™ RT Reagent Kit with gDNA Eraser (#RR047A, Takara). Reverse transcription quantitative real-time PCR (RT-qPCR) was performed on a Roche LightCycler® 480 system with TransStart® Tip Green qPCR SuperMix (#AQ141-01, TransGen) for miRNAs and TB Green™ Premix (#RR820A, Takara) for mRNAs. All reactions were run in triplicate under the following cycling conditions: 94 °C for 30 s; 40 cycles of 95 °C for 5 s and 60 °C for 30 s. The $2^{-\Delta\Delta_{CT}}$ method was applied to calculate relative expression levels using glyceraldehyde-3-phosphate dehydrogenase (GAPDH) as the control for mRNA normalization and miR-26a/30d/152 for miRNA normalization. The

sequences of specific primers are presented in Supplementary Table 1.

ELISA

Protein expression levels of RSAD2, CST6, and KRT77 were quantified using commercial ELISA kits from Jiangsu Meimian Biotechnology Co., Ltd. Skin tissues were homogenized in RIPA buffer containing 1% PMSF using a high-throughput homogenizer with steel beads (40 Hz, 30 s, 6 cycles), followed by centrifugation at 15,000 ×*g* for 15 min at 4 °C. The supernatant was collected for analysis. Total protein concentration was determined via bicinchoninic acid assay. For ELISA, each well was loaded with 50 μL of standard or diluted sample, followed by 100 μL enzyme conjugate and incubation at 37 °C for 60 min. After washing, 50 μL of chromogen A and B were added and incubated at 37 °C for 15 min in the dark. The reaction was stopped with 50 μL stop solution, and absorbance was measured at 450 nm. Protein concentrations were calculated based on standard curves.

Plasmid construction and validation

To validate the targeting relationships between mmu-miR-15b-5p, mmu-miR-31-5p, mmu-miR-1983 and their putative target genes (*Rsad2, Cst6, Krt77*), fragments containing the predicted binding sites within the 3' UTR regions were amplified using high-fidelity PCR with primers designed based on GenBank reference sequences. Genomic DNA was extracted from mouse skin tissue using a commercial kit (#K0512, Thermo), after which the amplified products were purified by gel extraction. The purified fragments were ligated into either the pBM20s or PmirGLO vector using T4 DNA ligase. Ligation products were then transformed into T-Fast competent cells, followed by heat shock at 42 °C for 90 s. Positive clones were selected on LB agar plates containing ampicillin and cultured overnight at 37 °C. Subsequently, plasmids were extracted using a plasmid miniprep kit (#K210003, Thermo Fisher) and validated by double restriction digestion with XbaI (#ER0682, Thermo Fisher) and XhoI (#ER0691, Thermo Fisher). Finally, plasmid concentrations were measured using a NanoDrop One spectrophotometer and stored at -20°C for further use.

Dual-luciferase reporter assay

HEK293 cells were maintained in Dulbecco's Modified Eagle Medium (DMEM) supplemented with 10% fetal bovine serum and 1% P/S at 37 °C in a 5% CO_2 atmosphere. For transfection, cells were seeded into 24-well plates and grown until 70%-80% confluency. Wild-type or mutant reporter plasmids, along with corresponding miRNA mimics, were co-transfected into the cells using Lipofectamine 3000 (#L3000008, Thermo) according to the manufacturer's protocol. After 6 h of transfection, the medium was replaced with fresh complete medium, and cells were further incubated for 24 h. Subsequently, luciferase activity was assessed using the Dual-Luciferase® Reporter Assay System (#E1910, Promega). Briefly, cells were lysed with 1× Passive Lysis Buffer, and firefly luciferase activity was measured immediately after adding the substrate. Then, Renilla luciferase activity was quantified following the addition of Stop & Glo® Reagent. The relative luciferase activity was calculated as the ratio of firefly to Renilla luminescence.

Validation of the miRNA-mRNA-Protein triad system for wound age estimation

To evaluate the accuracy of the mathematical models established using the miRNA-mRNA-Protein Triad System, an additional 33 male C57BL/6J mice were employed (n = 3 per time point per group). Skin tissues were collected at the predetermined post-injury intervals, followed by extraction and quantification of miRNA, mRNA, and protein levels for model validation. Furthermore, to assess the stability of the model under postmortem conditions, 60 mice were used, including 15 controls and 45 subjected to incised wounds. The injured mice were euthanized at 1, 5, and 13 days post-injury (n = 15 per group). The carcasses were placed in a climate chamber maintained at 25 ± 2 °C and 55% ± 3% humidity. Skin samples were collected at postmortem intervals of 0, 1.5, 3, 4.5 and 6 days (n = 3 per time point per group). The expression levels of the triad system molecules were measured and input into the optimal mathematical model to evaluate the impact

of postmortem changes on the accuracy of wound age estimation. Of note, for the mmu-miR-15b-5p/Rsad2/RSAD2 triad, the 13 d post-injury time point was collected but excluded from the final analysis because its optimal pre-injury window is within 9 d (see **RESULTS**).

Machine learning

The dataset was randomly split into a training set (50% of samples) and a test set (50% of samples). Parameters were optimized via cross-validation to reduce overfitting. Model performance was evaluated using the coefficient of determination (R2), root mean square error (RMSE), and mean absolute error (MAE). RF and XGBoost were selected due to their proven robustness with small sample sizes and their capability to capture non-linear relationships without requiring strong parametric assumptions. Machine learning models were implemented in Python. RF was applied using the "RandomForest Regressor" package, and XGBoost was implemented using the "XGBRegressor" package.

Statistical analysis

Statistical analyses were performed using GraphPad Prism 9, and Python 3.7.6. Univariate and multivariate linear regression models were conducted in GraphPad-Prism. Data are presented as mean ± standard deviation (SD). Comparisons between groups were performed using one-way analysis of variance (ANOVA) or two-tailed unpaired Student's *t*-test. $P < 0.05$ was considered statistically significant.

RESULTS

To explore the temporal expression patterns of miRNAs and mRNAs during skin wound healing, we performed small RNA sequencing and RNA sequencing on skin samples collected from the wound edge at different post-injury intervals (12 h, 3 d, 7 d, and 14 d), as well as from normal control skin. PCA revealed distinct clustering patterns for both miRNAs and mRNAs. For miRNAs, the normal control and 12 h groups showed partial overlap, while samples from 3 d, 7 d, and 14 d were clearly separated from the control group and from each other, indicating dynamic changes in miRNA expression during wound healing [Figure 1A]. Similarly, PCA of mRNA expression profiles demonstrated a clear separation between normal control and all wound time points, with a progressive temporal shift in the clustering pattern [Figure 1B]. Differential expression analysis was further performed, and a total of 313 unique differentially expressed miRNAs were identified in wounded skin compared to normal controls. The number of differentially expressed miRNAs increased gradually from 12 h to 7 d and decreased slightly at 14 d [Figure 1C and D]. For mRNAs, 4,737 unique differentially expressed transcripts were detected in wounded skin relative to normal controls. The number of differentially expressed mRNAs increased progressively from 12 h to 14 d, with the highest number observed at 14 d post-injury [Figure 1E and F]. The number of differentially expressed mRNAs increased progressively from 12 h to 14 d, with the highest number observed at 14 d post-injury [Figure 1D]. These results indicate that both miRNAs and mRNAs undergo substantial and time-dependent changes during skin wound healing, providing a comprehensive expression landscape for further analysis.

We next visualized the global expression profiles by generating heatmaps for the top five differentially expressed miRNAs and mRNAs across normal skin and each post-injury time point [Figure 2A and B]. At 12 h post-injury, the most highly expressed mRNAs were enriched for chemokines and inflammation-related genes such as *Il-1β* and *Cxcl10*, indicating an early inflammatory response. In contrast, by 14 d, transcripts involved in tissue remodeling, including *Krt28* and *Tchh*, became predominant, reflecting the progression of wound healing [Figure 2B]. Among the differentially expressed miRNAs, mmu-miR-15b-5p, mmu-miR-31-5p, and mmu-miR-1983 exhibited progressively increasing expression from 12 h to 14 d, displaying monotonic rather than biphasic expression patterns that are particularly suitable for wound age estimation [Figure 2A and Supplementary Figure 1A]. For mRNAs, the corresponding target genes *Rsad2*, *Cst6*, and *Krt77* showed opposite trends, with expression levels decreasing over time [

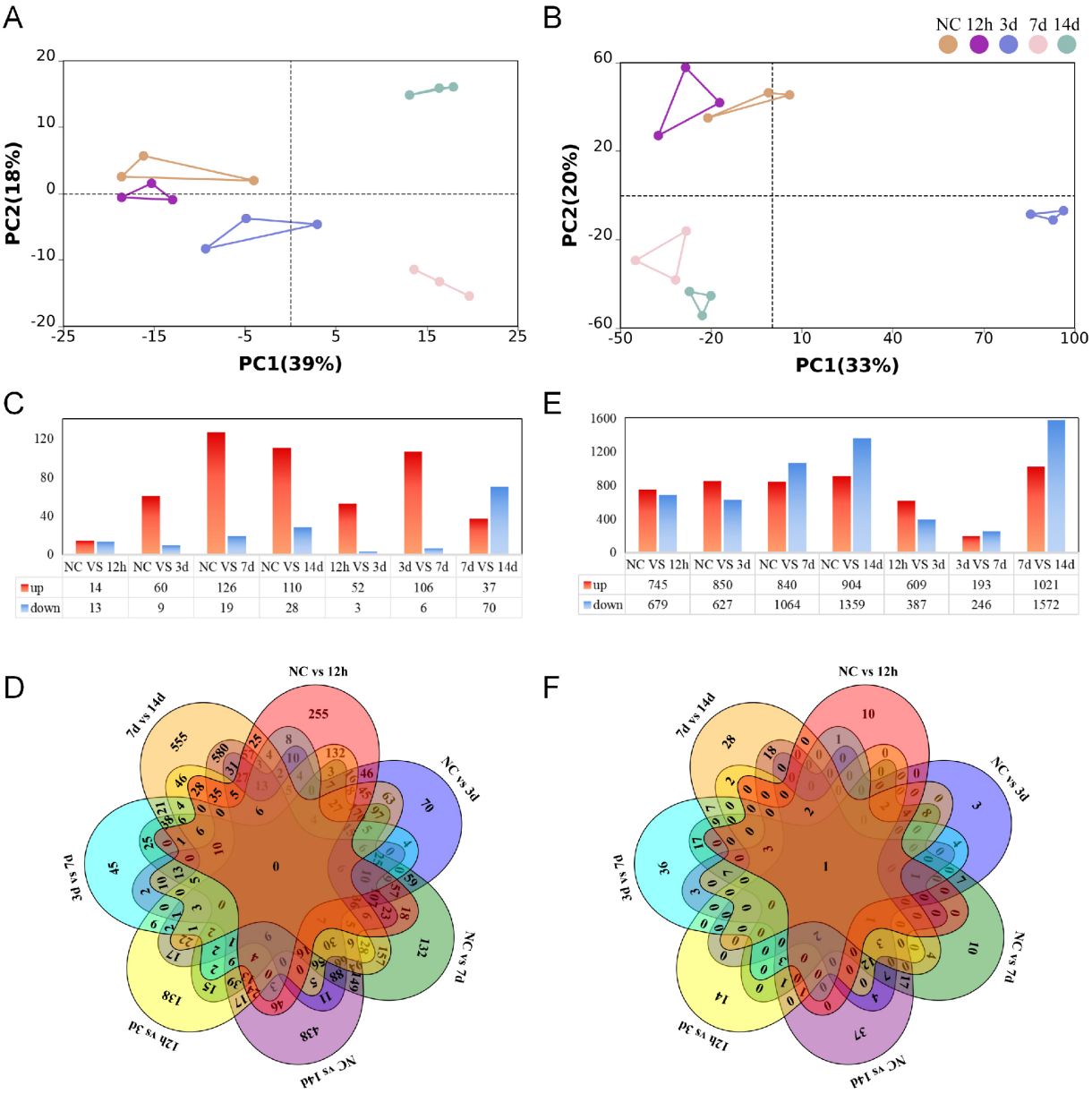

Figure 1. High-throughput sequencing profiles of miRNAs and mRNAs during skin wound healing. (A and B) PCA scatter plot of (A)miRNA and (B)mRNA sequencing data from normal control and wounded skin at indicated post-injury time points, $n = 3$; (C and D) Differential expression analysis of miRNAs; (C) Bar chart showing the number of differentially expressed miRNAs in wounded skin compared to normal controls at each post-injury time point, $|\log_2 FC| > 1$, adjusted $P < 0.05$. (D) Petal plot illustrating the overlap of differentially expressed miRNAs across different post-injury time points; (E and F) Differential expression analysis of mRNAs; (E) Bar chart showing the number of differentially expressed mRNAs in wounded skin compared to normal controls at each post-injury time point, $|\log_2 FC| > 1$, adjusted $P < 0.05$; (F) Petal plot illustrating the overlap of differentially expressed mRNAs across different post-injury time points. PCA: Principal component analysis; FC: fold change.

Supplementary Figure 1B]. Temporal expression patterns were further analyzed using STEM. The three miRNAs were clustered together in cluster 2, characterized by progressively increasing expression [Figure 2C], while their target mRNAs were enriched in cluster 9, showing a progressively decreasing trajectory (*Cst6*, *Krt77*), and *Rsad2* peaking at 12 h and declining thereafter were enriched in cluster 9 [Figure 2D and E]. These coherent temporal trajectories suggested potential functional coupling between these miRNA-mRNA pairs. To systematically characterize the regulatory interactions, we constructed a miRNA-mRNA regulatory network by integrating miRNA target predictions (TargetScan, RNAhybrid, and

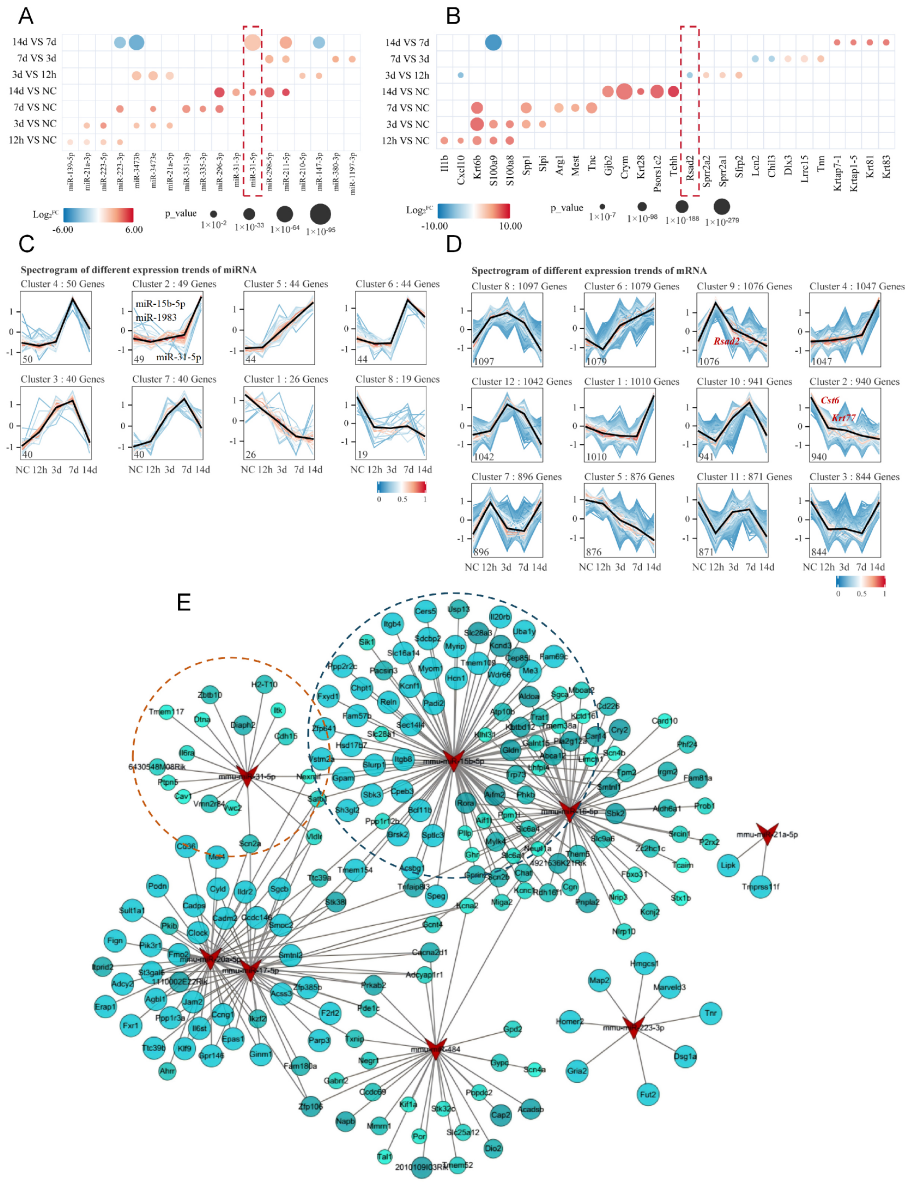

Figure 2. Identification of key differentially expressed miRNAs and mRNAs and construction of the miRNA-mRNA regulatory network. (A and B) Heatmaps showing the top five differentially expressed miRNAs (A) and mRNAs (B) in normal skin and at indicated post-injury time points. Circle size represents statistical significance, and color intensity indicates the magnitude of differential expression; (C and D) STEM analysis of temporal expression patterns of differentially expressed miRNAs (C) and mRNAs (D). Color intensity represents $\log_2$FC values, with each profile depicting a distinct expression trajectory; (E) miRNA-mRNA regulatory network during skin wound healing. Triangles represent miRNAs, and circles represent mRNAs. Circle color intensity reflects the PCC, and circle size indicates statistical significance. Only negatively correlated pairs are shown. PCC < -0.7, $P < 0.05$. STEM: Short Time-series Expression Miner; FC: fold change; PCC: Pearson correlation coefficient.

miRanda) with differentially expressed mRNAs from RNA-seq data. Regulatory pairs with a PCC < -0.7 and $P < 0.05$ were considered significant. As shown in Figure 2E, the network comprised 150 miRNAs and 763 mRNAs, forming 1,573 negative regulatory edges [Table 1]. mmu-miR-15b-5p occupied a central position with the highest degree (degree = 93), and mmu-miR-31-5p also displayed extensive nodal interactions, targeting multiple downstream genes. Given the favorable monotonic expression patterns of these three miRNAs and their target mRNAs, along with their central positions in the regulatory network and their consistent inverse expression relationships, we selected mmu-miR-15b-5p/*Rsad2*, mmu-miR-31-5p/*Cst6*, and mmu-miR-1983/*Krt77* for subsequent experimental validation.

Table 1. Number of DEmiRNA-mRNA regulatory networks in the process of skin wound injury

Wound Age	miRNA-mRNA		
	DEmiRNA	DEmRNA	DEmiRNA-mRNA
12h *vs.* NC	15	1424	473
3d *vs.* NC	56	1477	1905
7d *vs.* NC	112	1904	6421
14d *vs.* NC	100	2263	7928
3d *vs.* 12h	40	997	711
7d *vs.* 3d	81	439	929
14d *vs.* 7d	66	2593	2968
14d *vs.* 7d *vs.* 3d *vs.* 12h *vs.* NC	208	4737	16629
14d *vs.* 7d *vs.* 3d *vs.* 12h *vs.* NC*	150	763	1573

* PCC < -0.7, $P < 0.05$. PCC: Pearson correlation coefficient.

Following the identification of mmu-miR-15b-5p/*Rsad2*, mmu-miR-31-5p/*Cst6*, and mmu-miR-1983/*Krt77* as candidate regulatory axes with favorable temporal patterns and network centrality, we proceeded to validate their expression dynamics and regulatory relationships. RT-qPCR analysis revealed that all three miRNAs exhibited progressively increasing expression after injury, albeit with distinct peak times: mmu-miR-15b-5p peaked at day 9, mmu-miR-31-5p at day 17, and mmu-miR-1983 at day 13, followed by gradual declines [Figure 3A-]. In contrast, the corresponding target mRNAs-*Rsad2*, Cst6, and *Krt77*-displayed overall decreasing trends, with *Rsad2* showing a transient elevation from 12 h to 1 d, while *Cst6* and *Krt77* declined progressively from 1 d onward, reaching their lowest levels between 7 d and 9 d before partial recovery [Figure 3D-F]. Dual-luciferase reporter assays confirmed direct targeting relationships: co-transfection with miRNA mimics significantly reduced luciferase activity for wild-type 3' untranslated region (3'UTR) constructs, but not for mutant constructs, validating *Rsad2*, Cst6, and *Krt77* as direct targets of mmu-miR-15b-5p, mmu-miR-31-5p, and mmu-miR-1983, respectively [Figure 3G-I]. Finally, ELISA quantification of the corresponding proteins across the wound healing time course revealed expression patterns consistent with their respective mRNAs [Figure 3J-L]. Integrating these findings, we constructed three 'miRNA-mRNA-protein' triads-mmu-miR-15b-5p/*Rsad2*/RSAD2, mmu-miR-31-5p/*Cst6*/CST6, and mmu-miR-1983/*Krt77*/KRT77-each demonstrating coordinated inverse expression relationships, supporting their potential utility as integrated biomarkers for wound age estimation.

To evaluate the potential of these biomarkers for quantitative wound age estimation, we first assessed the performance of individual components within each triad using univariate linear regression. For each miRNA, target mRNA, and protein, we fitted linear models within their optimal post-injury time windows [Table 2]. As shown in Figure 4A-C and Table 2, mmu-miR-15b-5p exhibited a strong linear correlation with wound age within the first 9 days ($R^2 = 0.9657$), whereas *Rsad2* mRNA and RSAD2 protein showed weaker negative correlations ($R^2 = 0.5401$ and 0.7100, respectively). Similar patterns were observed for the other two triads: miRNAs consistently outperformed their corresponding mRNAs and proteins in linear fit, with mmu-miR-31-5p achieving an R^2 of 0.8490 over 17 days [Figure 4D-F], and mmu-miR-1983 reaching 0.9498 over 13 days [Figure 4G-I]. The moderate predictive power of single mRNA or protein markers highlighted the need for multi-parameter integration.

Given the limitations of single-biomarker approaches, we next constructed multivariate models incorporating all three components within each triad. Multivariate linear regression substantially improved model fit compared to univariate approaches, with adjusted R^2 values reaching 0.9813 (within 9 d) for the

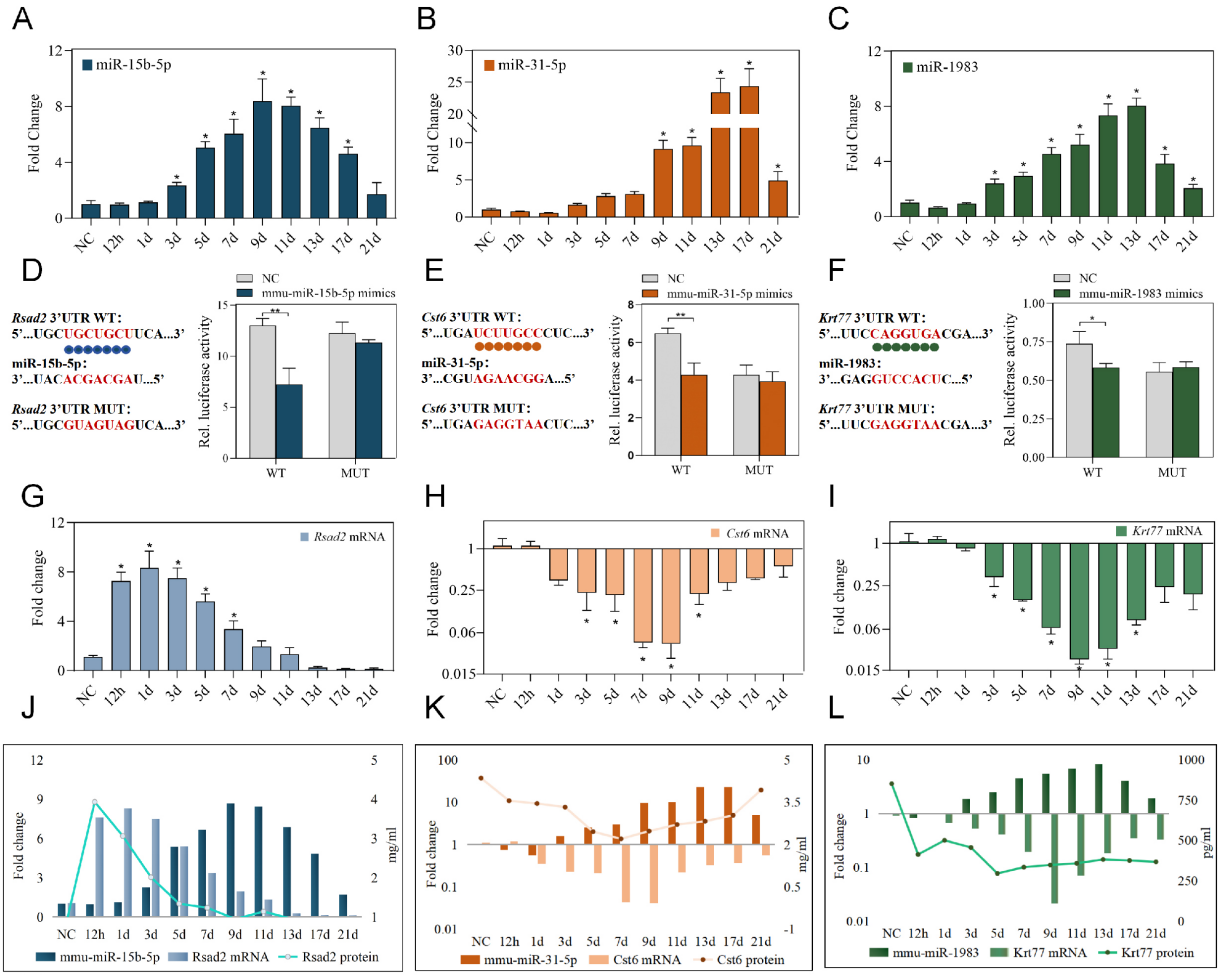

Figure 3. Validation of miRNA-mRNA-protein triads during skin wound healing. (A-C) Relative expression levels of mmu-miR-15b-5p (A); mmu-miR-31-5p (B); and mmu-miR-1983 (C) in normal skin and at indicated post-injury time points, as determined by RT-qPCR. Expression levels were normalized to NC group (set as 1). Data were analyzed by one-way ANOVA followed by Tukey's post-hoc test; n = 3, $^{*}P < 0.05$ *vs.* NC group; (D-F) Schematic diagrams showing the predicted binding sites of mmu-miR-15b-5p within the 3'UTR of *Rsad2* mRNA (D); mmu-miR-31-5p within the 3'UTR of *Cst6* mRNA (E); and mmu-miR-1983 within the 3'UTR of *Krt77* mRNA (F), along with the corresponding mutant sequences. Bar graphs represent the dual-luciferase reporter activities following co-transfection with wild-type or mutant constructs and corresponding miRNA mimics. Data are presented as mean ± SD, analyzed by unpaired t-test, n = 3, $^{*}P < 0.05$ and $^{**}P < 0.01$ *vs.* NC group; (G-I) Relative expression levels of *Rsad2* mRNA (G), *Cst6* mRNA (H), and *Krt77* mRNA (I) in normal skin and at indicated post-injury time points, as determined by RT-qPCR. Expression levels were normalized to NC group (set as 1). Data were analyzed by one-way ANOVA followed by Tukey's post-hoc test; n = 3, $^{*}P < 0.05$ vs. NC group; (J-L) Expression patterns of the mmu-miR-15b-5p/*Rsad2*/RSAD2 triad (J), mmu-miR-31-5p/ *Cst6*/CST6 triad (K), and mmu-miR-1983/*Krt77*/KRT77 triad (L) during skin wound healing. The expression dynamics of each miRNA, its target mRNA, and the corresponding protein are shown to illustrate the coordinated inverse relationships within each triad. WT: Wild type; MUT: mutant; NC: ANOVA: analysis of variance; RT-qPCR: reverse transcription quantitative real-time PCR; 3'UTR: 3' untranslated region; SD: standard deviation.

mmu-miR-15b-5p/*Rsad2*/RSAD2 triad, 0.9121 (within 13 d) for mmu-miR-31-5p/*Cst6*/CST6, and 0.9643 (within 13 d) for mmu-miR-1983 /*Krt77*/KRT77. External validation confirmed acceptable predictive errors (MAE: 1.240, 1.299, and 0.872, respectively) [Table 3 and Figure 5A-C]. Given the non-linear dynamics of wound healing, we further explored machine learning approaches using RF and XGBoost [Tables 4-6]. For the mmu-miR-15b-5p/*Rsad2*/RSAD2 triad, both RF and XGBoost achieved optimal performance within 9 days post-injury [Figure 5D and E]. Within this window, RF achieved an R^2 of 0.861, RMSE of 1.20, and MAE of 0.87, while XGBoost showed comparable fit (R^2 = 0.861, RMSE = 1.20) with a slightly lower MAE (0.72). For the mmu-miR-31-5p/*Cst6*/CST6 triad, optimal performance was observed within 13 days [Figure 5F and G]. RF yielded an R^2 of 0.926, RMSE of 1.22, and MAE of 0.94, whereas XGBoost performed slightly

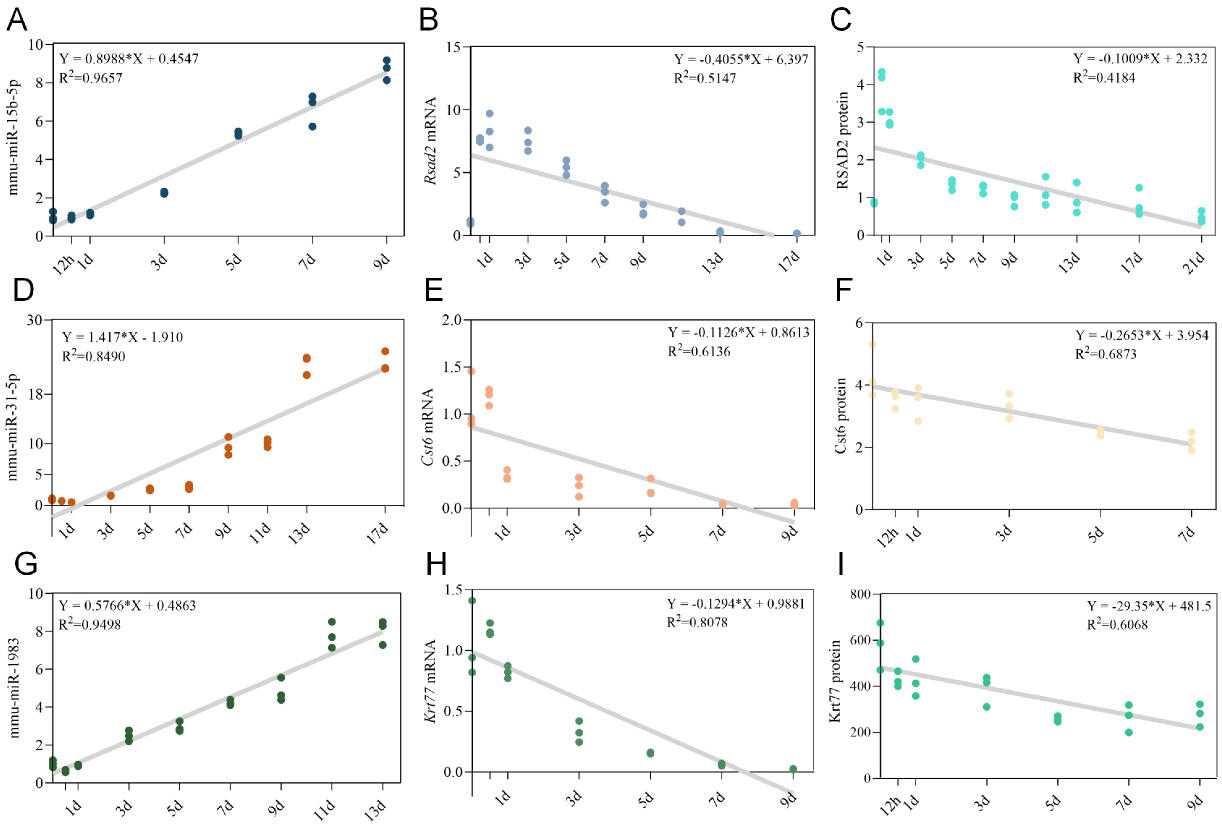

Figure 4. Univariate linear regression models for individual biomarkers in wound age estimation. (A-C) Optimal univariate linear regression models for mmu-miR-15b-5p (A), *Rsad2* mRNA (B), and RSAD2 protein (C) within the mmu-miR-15b-5p/*Rsad2*/RSAD2 triad. The best-fit linear equations and coefficients of determination (R^2) were determined within the optimal post-injury time windows; (D-F) Optimal univariate linear regression models for mmu-miR-31-5p (D), Cst6 mRNA (E), and CST6 protein (F) within the mmu-miR-31-5p/*Cst6*/CST6 triad; (G-I) Optimal univariate linear regression models for mmu-miR-1983 (G), Krt77 mRNA (H), and KRT77 protein (I) within the mmu-miR-1983/*Krt77*/KRT77 triad.

Table 2. Univariate linear regression models for individual biomarkers

Model	R^2	Wound age	Equation
mmu-miR-15b-5p	0.9657	9d	Y = 0.8988X + 0.4547
Rsad2 mRNA	0.5401	9d	Y = -0.3453X + 6.124
Rsad2 Protein	0.710	9d	Y = -0.2766X + 3.734
mmu-miR-31-5p	0.8490	17d	Y = 1.417X - 1.910
Cst6 mRNA	0.6136	9d	Y = -0.1126X + 0.8613
Cst6 Protein	0.6873	7d	Y = -0.2653X + 3.954
mmu-miR-1983	0.9498	13d	Y = 0.5766X + 0.4863
Krt77 mRNA	0.8078	9d	Y = -0.1294X + 0.9881
Krt77 Protein	0.6068	9d	Y = -29.35X + 481.5

better (R^2 = 0.942, RMSE = 1.09, MAE = 0.74). For the mmu-miR-1983/*Krt77*/KRT77 triad, the optimal window was 13 days [Figure 5H and I]. XGBoost substantially outperformed RF, with R^2 = 0.941 (*vs.* 0.844), RMSE = 1.10 (*vs.* 1.78), and MAE = 0.86 (*vs.* 1.28). Collectively, these results demonstrate that the triad system, when combined with appropriate multivariate modeling strategies, significantly improves the accuracy of wound age estimation. Among the two machine learning algorithms, XGBoost generally provided better or comparable performance, particularly for the mmu-miR-1983/*Krt77*/KRT77 triad.

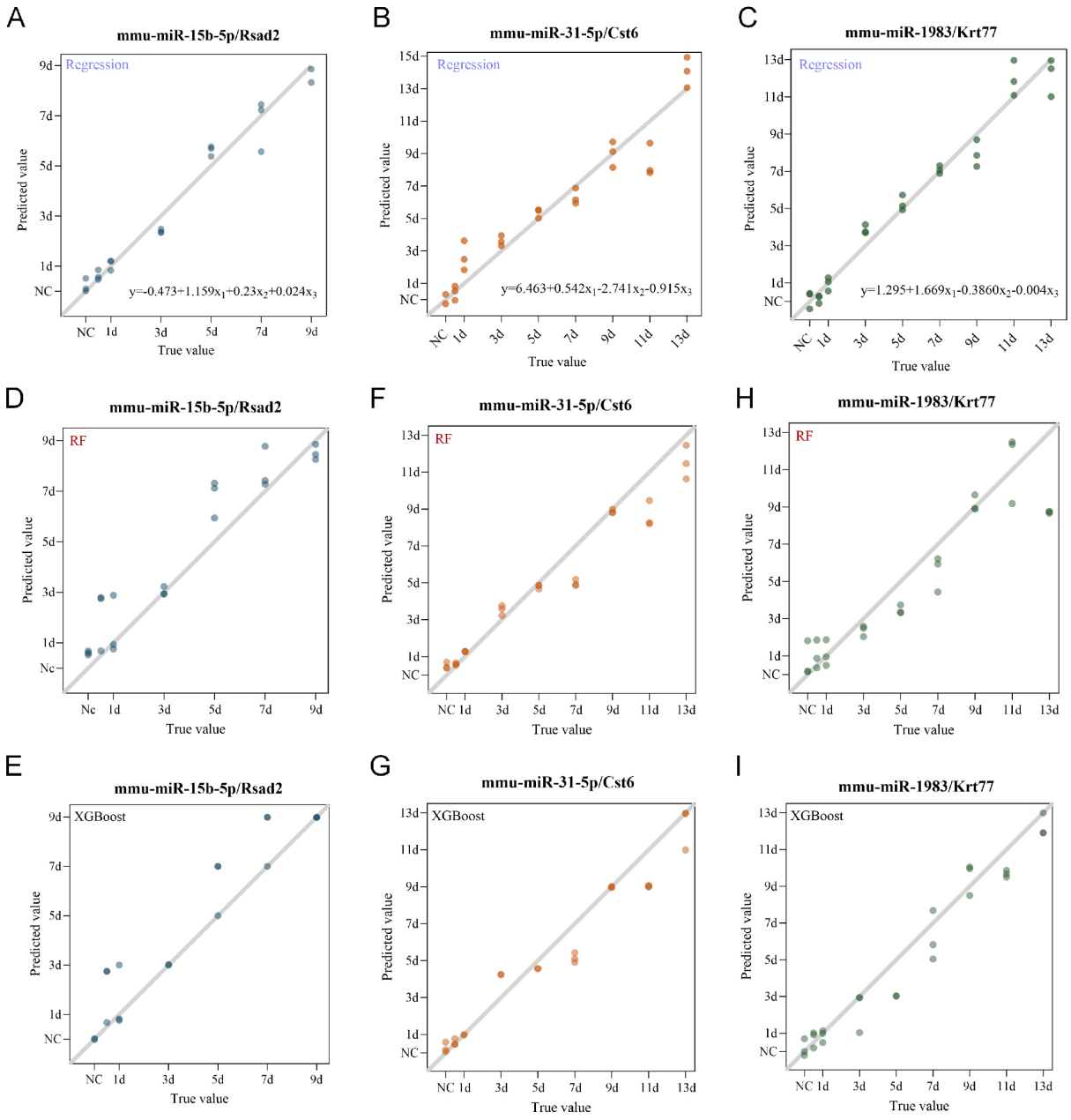

Figure 5. Multivariate regression and machine learning models for wound age estimation using the triad system. (A-C) Optimal multivariate linear regression models for the mmu-miR-15b-5p/*Rsad2*/RSAD2 triad (A), mmu-miR-31-5p/*Cst6*/CST6 triad (B), and mmu-miR-1983/*Krt77*/KRT77 triad (C). X_1, X_2, and X_3 represent the expression levels of miRNA, target mRNA, and corresponding protein, respectively; (D and E) Random Forest (D) and XGBoost (E) models for the mmu-miR-15b-5p/*Rsad2*/RSAD2 triad, constructed within the optimal post-injury windows; (F and G) Random Forest (F) and XGBoost (G) models for the mmu-miR-31-5p/*Cst6*/CST6 triad, constructed within the optimal post-injury windows; (H and I) Random Forest (H) and XGBoost (I) models for the mmu-miR-1983/*Krt77*/KRT77 triad, constructed within the optimal post-injury windows.

Table 3. Multivariate linear regression models for the miRNA-mRNA-protein triads

Model	R^2	Adjust R^2	F	Significance	RMSE	MAE
mmu-miR-15b-5p/*Rsad2*/RSAD2	0.9841	0.9813	350.7	$P < 0.001$	1.8565	1.240
mmu-miR-31-5p/*Cst6*/CST6	0.9222	0.9121	90.89	$P < 0.001$	1.5998	1.299
mmu-miR-1983/*Krt77*/KRT77	0.9684	0.9643	234.9	$P < 0.001$	0.8977	0.872

RMSE: Root mean square error; MAE: mean absolute error.

Table 4. RF and XGBoost regression models for the mmu-miR-15b-5p/*Rsad2*/RSAD2 triad

Wound Age	RF			XGBoost		
	R^2	RMSE	MAE	R^2	RMSE	MAE
21d	0.843	2.64	2.09	0.79	3.05	2
17d	0.815	2.36	1.81	0.848	2.15	1.48
13d	0.915	1.31	1.06	0.888	1.51	1.05
11d	0.89	1.26	1.01	0.89	1.29	0.88
9d	0.861	1.2	0.87	0.861	1.2	0.72

RF: Random Forest; RMSE: root mean square error; MAE: mean absolute error.

Table 5. RF and XGBoost regression models for the mmu-miR-31-5p/*Cst6*/CST6 triad

Wound age	RF			XGBoost		
	R^2	RMSE	MAE	R^2	RMSE	MAE
21d	0.887	2.24	1.38	0.874	2.36	1.68
17d	0.952	1.2	0.92	0.915	1.6	1.23
13d	0.926	1.22	0.94	0.942	1.09	0.74

RF: Random Forest; RMSE: root mean square error; MAE: mean absolute error.

Table 6. RF and XGBoost regression models for the mmu-miR-1983/*Krt77*/KRT77 triad

Wound age	RF			XGBoost		
	R^2	RMSE	MAE	R^2	RMSE	MAE
21d	0.481	4.8	2.62	0.324	5.48	3.14
17d	0.805	2.43	1.5	0.776	2.6	1.37
13d	0.844	1.78	1.28	0.941	1.1	0.86

RF: Random Forest; RMSE: root mean square error; MAE: mean absolute error.

Having established the predictive performance under optimal conditions, we next assessed whether this triad system could withstand postmortem degradation - a critical consideration for forensic applications. To evaluate the robustness of the triad system against postmortem degradation, we assessed model performance using samples subjected to different postmortem intervals (PMI). Skin tissues were collected from normal controls and at 1 d, 5 d, and 13 d post-injury. Samples were maintained at 25 ± 2 °C and 55% ± 3% humidity, and collected at PMI of 0, 1.5, 3, 4.5 d and 6d (PMI = 6 d samples were collected but not included in data analysis due to serious degradation. All results below are based on PMI ≤ 4.5d). Expression levels were input into the established multivariate models (multivariate linear regression, RF, and XGBoost) to evaluate the impact of postmortem changes on estimation accuracy [Figure 6 and Tables 7-9]. The mmu-miR-31-5p/*Cst6*/CST6 triad showed the greatest resistance to postmortem interference. At PMI = 0, all three models performed well (R^2 = 0.858-0.876). Performance remained stable with increasing PMI: at PMI = 1.5 d, RF and XGBoost achieved R^2 = 0.956 and 0.960 with MAE as low as 0.77 and 0.60; at PMI = 3 d, XGBoost maintained R^2 = 0.932 (MAE = 1.04); and even at PMI = 4.5 d, XGBoost retained R^2 = 0.923 (MAE = 1.16). When all PMI data were combined, XGBoost yielded the best overall performance (R^2 = 0.908, RMSE = 1.56, MAE = 1.05), indicating that this triad retains considerable predictive power under postmortem conditions. In contrast, the other two triads exhibited substantial performance degradation with increasing PMI, with predictive performance declining notably even at early PMI time points [Tables 7-9]. Collectively, these results indicate that the robustness of the triad system against postmortem changes varies considerably across triads. The mmu-miR-31-5p/*Cst6*/CST6 triad demonstrated superior resistance to postmortem

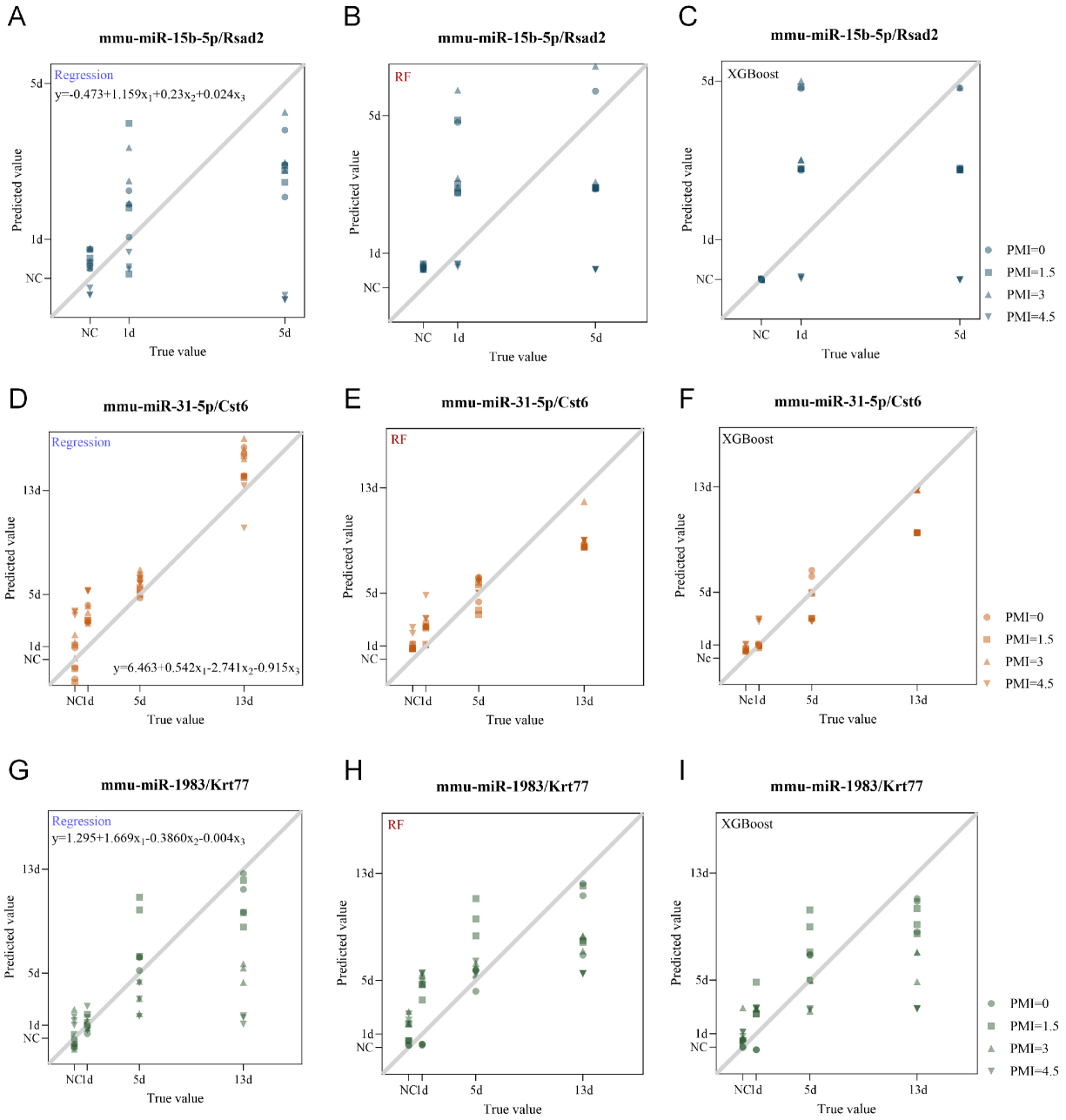

Figure 6. Figure 6 . Evaluation of the triad system robustness against postmortem changes; (A-C) Scatter plots showing predicted versus actual wound age for test set samples of the mmu-miR-15b-5p/*Rsad2*/RSAD2 triad across different postmortem intervals (PMI = 0, 1.5, 3, and 4.5 d) at indicated post-injury time points (NC, 1 d, 5 d), using multivariate linear regression (A), Random Forest (B), and XGBoost (C); (D-F) Scatter plots showing predicted versus actual wound age for test set samples of the mmu-miR-31-5p/*Cst6*/CST6 triad across different PMI (0, 1.5, 3, and 4.5 d) at indicated post-injury time points (NC, 1 d, 5 d, and 13 d), using multivariate linear regression (D), Random Forest (E), and XGBoost (F); (G-I) Scatter plots showing predicted versus actual wound age for test set samples of the mmu-miR-1983/*Krt77*/KRT77 triad across different PMI (0, 1.5, 3, and 4.5 d) at indicated post-injury time points (NC, 1 d, 5 d, and 13 d), using multivariate linear regression (G), Random Forest (H), and XGBoost (I). The black line represents the y = x diagonal, and dots are represented by different shapes according to PMI. NC: PMI: postmortem intervals.

degradation, particularly when combined with XGBoost, whereas the other two triads were more susceptible to postmortem interference. These findings underscore the importance of selecting appropriate biomarker sets and modeling strategies for wound age estimation in postmortem settings.

DISCUSSION

Accurate estimation of skin wound age remains a critical challenge in forensic pathology, as traditional single-marker approaches are often compromised by various pre- and post-mortem factors[26,27]. This study aimed to overcome these limitations by integrating multi-omics technologies with machine learning algorithms to develop a novel, reliable method for wound age estimation. We successfully constructed and validated a "miRNA-mRNA-protein triad system" based on mmu-miR-15b-5p/*Rsad2*/RSAD2, mmu-miR-31-5p/*Cst6*/CST6, and mmu-miR-1983/*Krt77*/KRT77. For each biomarker set, we identified optimal mathematical models, and systematically evaluated the impact of postmortem changes on estimation accuracy. Our results demonstrate that this integrated strategy enhances both accuracy and robustness, offering a new methodological framework for forensic practice.

Skin wound healing is a complex, multi-phase process involving coordinated regulation of numerous genes and signaling pathways. Using next-generation sequencing, we characterized the temporal expression landscapes of miRNAs and mRNAs during wound healing, identifying 313 differentially expressed miRNAs and 4,737 differentially expressed mRNAs. Consistent with previous studies[28,29], both miRNA and mRNA expression exhibited time-dependent patterns, with monotonic expression trajectories - such as those exhibited by mmu-miR-15b-5p, mmu-miR-31-5p, and mmu-miR-1983 - being particularly advantageous for wound age estimation. By integrating three complementary miRNA target prediction algorithms with our RNA-seq data, we constructed a robust miRNA-mRNA regulatory network. The centrality of mmu-miR-15b-5p (degree = 93) and mmu-miR-31-5p within this network, together with their monotonic expression patterns, supported their selection as candidate biomarkers. This network-based approach not only improved prediction accuracy but also provided insight into the molecular architecture underlying wound healing.

The biological relevance of the selected miRNA-mRNA axes is supported by existing literature. mmu-miR-15b-5p, a member of the miR-15 family, has been implicated in regulating apoptosis, proliferation, angiogenesis, and inflammation[30-32]. Its target, *Rsad2,* is an interferon-stimulated gene involved in antiviral responses and modulation of type I interferon signaling[33-36]. The inverse expression pattern observed in our study suggests a potential regulatory axis linking miRNA-mediated suppression of inflammatory responses to wound repair dynamics. Similarly, mmu-miR-31-5p has been shown to promote re-epithelialization via RAS/MAPK signaling and is associated with hypertrophic scar formation through HIF-1α pathway activation[37]. Its target, Cst6 (cystatin M/E), is predominantly expressed in skin and localizes to the suprabasal layer of healing epidermis[38], consistent with our observed expression pattern. Although mmu-miR-1983 and its target Krt77 have been less characterized in wound healing contexts, their monotonic expression trajectories and network centrality suggest functional relevance warranting further investigation.

Given the limitations of single-marker approaches, we next evaluated the performance of individual biomarkers and then constructed multivariate models incorporating all three components within each triad. Univariate linear regression revealed that while miRNAs exhibited strong linear correlations with wound age (R^2 = 0.849-0.966), their corresponding mRNAs and proteins showed weaker predictive power (R^2 = 0.540-0.808). Multivariate linear regression substantially improved model fit, with adjusted R^2 values reaching 0.912-0.981, supporting the notion that functionally linked biomarkers provide more reliable estimates when analyzed collectively. Considering the non-linear dynamics of wound healing, we further explored machine learning approaches (RF and XGBoost). Notably, the optimal model varied across triads, reflecting distinct molecular dynamics. For the mmu-miR-15b-5p/*Rsad2*/RSAD2 triad, both models performed comparably within the 9 d window. For the mmu-miR-31-5p/*Cst6*/CST6 triad, XGBoost yielded better fit (R^2 = 0.942 *vs.* 0.926), while for the mmu-miR-1983/*Krt77*/KRT77 triad, XGBoost substantially

Table 7. Model performance for the mmu-miR-31-5p/*Cst6*/CST6 triad under different PMI

PMI	Regression			RF			XGBoost		
	R^2	RMSE	MAE	R^2	RMSE	MAE	R^2	RMSE	MAE
0 d	0.858	1.93	1.68	0.876	1.8	1.49	0.84	2.05	1.44
1.5 d	0.915	1.49	1.28	0.956	1.07	0.77	0.96	1.02	0.6
3 d	0.799	2.29	1.99	0.882	1.76	1.33	0.932	1.33	1.04
4.5 d	0.661	2.98	2.58	0.737	2.62	2.19	0.923	1.42	1.16
Overall	0.809	2.24	1.88	0.788	2.36	1.84	0.908	1.56	1.05

PMI: Postmortem intervals; RF: Random Forest; RMSE: root mean square error; MAE: mean absolute error.

Table 8. Model performance for the mmu-miR-1983/*Krt77*/KRT77 triad under different PMI

PMI	Regression			RF			XGBoost		
	R^2	RMSE	MAE	R^2	RMSE	MAE	R^2	RMSE	MAE
0 d	0.943	1.22	0.83	0.859	1.92	1.17	0.876	1.81	1.36
1.5 d	0.705	2.78	1.92	0.492	3.65	3.16	0.651	3.02	2.53
3 d	0.343	4.15	2.77	0.532	3.5	3.06	0.487	3.67	2.69
4.5 d	-0.345	5.93	3.92	0.233	4.48	3.65	-0.056	5.26	3.63
Overall	0.412	3.92	2.36	0.529	3.51	2.76	0.489	3.66	2.55

PMI: Postmortem intervals; RF: Random Forest; RMSE: root mean square error; MAE: mean absolute error.

Table 9. Model performance for the mmu-miR-15b-5p/*Rsad2*/RSAD2 triad under different PMI

PMI	Regression			RF			XGBoost		
	R^2	RMSE	MAE	R^2	RMSE	MAE	R^2	RMSE	MAE
0 d	0.587	1.39	1.08	0.231	1.89	1.59	0.27	1.85	1.33
1.5 d	0.354	1.74	1.47	0.144	2	1.74	0.143	2	1.57
3 d	0.543	1.46	1.25	-0.007	2.17	1.79	0.187	1.95	1.41
4.5 d	-1.207	3.21	2.16	-0.456	2.61	1.78	-0.858	2.94	1.99
Overall	0.069	2.08	1.49	-0.022	2.18	1.73	-0.064	2.23	1.58

PMI: Postmortem intervals; RF: Random Forest; RMSE: root mean square error; MAE: mean absolute error.

outperformed RF (R^2 = 0.941 *vs.* 0.844). These differences can be attributed to the distinct characteristics of the two algorithms: RF may offer greater robustness against noise and overfitting through bootstrap aggregation and random feature selection, making it well-suited for datasets with high variability. In contrast, XGBoost iteratively optimizes residuals and incorporates regularization, which may enable higher predictive accuracy when underlying patterns are relatively consistent, particularly within shorter, well-defined time windows (9-13 d). These findings suggest that algorithm selection should be tailored to the intrinsic dynamics of the molecular markers rather than seeking a universal model.

A critical consideration for forensic applications is biomarker stability under postmortem conditions. To our knowledge, this study represents the first systematic evaluation of how postmortem changes affect the predictive accuracy of a multi-marker wound age estimation system. We found that the mmu-miR-31-5p/*Cst6*/CST6 triad exhibited reliable resistance to postmortem degradation, with XGBoost maintaining $R^2 > 0.92$ even at PMI = 4.5 d. In contrast, the other two triads showed substantial performance deterioration with increasing PMI. The greater stability of the mmu-miR-31-5p/*Cst6*/CST6 triad may reflect protective mechanisms such as the sequestration of miR-31-5p by RNA-binding proteins or extracellular vesicles, and the unique epidermal localization of CST6, which may limit its exposure to degradative enzymes[39-41]. Further mechanistic studies are needed to confirm these possibilities. Nevertheless, our findings provide a proof-of-concept that integrating multiple molecular layers with appropriate modeling strategies can partially mitigate postmortem effects.

Several limitations should be acknowledged. First, our study was conducted in a mouse model, and the molecular timeline of skin wound healing differs from that in humans. Although the selected triads are evolutionarily conserved, the specific time windows derived from this model may not directly translate to human cases; future validation using human skin wound samples is therefore necessary. Second, although the mmu-miR-31-5p/*Cst6*/CST6 triad demonstrated considerable stability under the tested postmortem conditions (25 ± 2 °C, 55% ± 3% humidity), these conditions represent only one controlled environmental scenario. In forensic practice, variable temperature, humidity, and other factors (e.g., insect activity, clothing) may differentially affect biomarker stability, and further validation under a broader range of postmortem conditions is needed. Third, although our sample sizes (n = 3-5 per time point) are consistent with exploratory studies, they are modest for training XGBoost. To mitigate overfitting, we used five-fold cross-validation. However, confidence intervals for performance metrics are expected to be wide due to the small dataset. Therefore, the current models should be considered proof-of-concept, and validation in larger cohorts is needed. Fourth, beyond 4.5 d postmortem, the "predictive performance" of all triads was compromised remarkably due to postmortem degradation, underscoring that tissue decomposition remains a major interfering factor for wound age estimation.

In summary, this study demonstrates that forensic wound age estimation is transitioning from traditional morphological and single-marker analyses toward a multi-marker, data-driven intelligent computational paradigm. By integrating high-throughput sequencing, systematic experimental validation, and advanced machine learning algorithms, we established a triad system that significantly improves estimation accuracy. Notably, we identified that different biomarker triads are best suited to different modeling approaches, and that postmortem robustness varies substantially across triads. These findings provide both an experimental basis for enhancing wound age estimation accuracy and a methodological framework for selecting appropriate biomarker-model combinations under challenging conditions.

DECLARATIONS

Authors' contributions

Conceptualization: Guan D, Zhao R, Wang L
Writing-original draft: Suo L, Yuan H, Fan Y
Investigation: Suo L, Yuan H, Fan Y

Data curation Suo L, Yuan H, Fan Y
Supervision: Guan D, Zhao R, Wang L
Writing - review & editing: Guan D, Zhao R, Wang L
Funding acquisition: Guan D, Zhao R, Wang L
Methodology: Du S, Mu S, Zhang F
Visualization: Du S, Mu S, Zhang F
Validation: Yang J, Sun J, Zhang F
All authors have read and approved the final manuscript.

Availability of data and materials

The raw data supporting the findings of this study are available from the corresponding author upon reasonable request.

AI and AI-assisted tools statement

Not applicable.

Financial support and sponsorship

This study was financially supported by the National Natural Science Foundation of China (Grant Nos. 81871529, 82271926)

Conflicts of interest:

Guan D and Zhao R are Editorial Board Members of *Legal Medicine Research*. Guan D and Zhao R were not involved in any steps of the editorial process, notably including reviewer selection, manuscript handling, and decision-making. The other authors declare that there are no conflicts of interest.

Ethical approval and consent to participate

All animal experiments were approved by the Animal Experiment Committee of China Medical University (Approval No. CMU2019119) and conducted in accordance with the National Institutes of Health Guide for the Care and Use of Laboratory Animals.

Consent for publication

Not applicable.

Supplementary Materials

Supplementary Materials

REFERENCES

1. Rodrigues M, Kosaric N, Bonham CA, Gurtner GC. Wound healing: a cellular perspective. *Physiol Rev.* 2019;99:665-706. DOI PubMed PMC
2. He L, Marneros AG. Macrophages are essential for the early wound healing response and the formation of a fibrovascular Scar. *Am J Pathol.* 2013;182:2407-17. DOI PubMed PMC
3. Cañedo-Dorantes L, Cañedo-Ayala M. Skin acute wound healing: a comprehensive review. *Int J Inflam.* 2019;2019:1-15. DOI PubMed PMC
4. Dang L, Feng N, An G, et al. Novel insights into wound age estimation: combined with "up, no change, or down" system and cosine similarity in python environment. *Int J Legal Med.* 2020;134:2177-86. DOI
5. Ahmed AE, Aljohani WF, Moafa AK, et al. Histological and immunohistochemical biomarkers for wound age estimation in human skin: a systematic review. *Cureus.* 2026;18:e100607. DOI PubMed PMC
6. Pennisi G, Torrisi M, Cocimano G, Esposito M, Salerno M, Sessa F. Vitality markers in forensic investigations: a literature review. *Forensic Sci Med Pathol.* 2022;19:103-16. DOI PubMed
7. Cecchi R, Ikeda T, Camatti J, Nosaka M, Ishida Y, Kondo T. Expression of matrix metalloproteinase-9 (MMP-9) in human skin within 1 hour after injury through immunohistochemical staining: a pilot study. *Int J Legal Med.* 2024;138:1985-90. DOI

8. Liu Z, Bian X, Luo L, et al. Spatiotemporal single-cell roadmap of human skin wound healing. *Cell Stem Cell.* 2025;32:479-498.e8. DOI
9. Dekoninck S, Blanpain C. Stem cell dynamics, migration and plasticity during wound healing. *Nat Cell Biol.* 2019;21:18-24. DOI PubMed PMC
10. Shaw TJ, Martin P. Wound repair: a showcase for cell plasticity and migration. *Curr Opin Cell Biol.* 2016;42:29-37. DOI PubMed
11. Aragona M, Dekoninck S, Rulands S, et al. Defining stem cell dynamics and migration during wound healing in mouse skin epidermis. *Nat Commun.* 2017;8:14684. DOI PubMed PMC
12. Zhao M, Ma X, Zuo Z, Wang Y, Fang Y, Sun Y. Microgravity modulates keratinocyte, fibroblast, and endothelial cell communication during wound healing. *Life Sci.* 2025;378:123842. DOI
13. Yampolsky M, Bachelet I, Fuchs Y. Reproducible strategy for excisional skin-wound-healing studies in mice. *Nat Protoc.* 2023;19:184-206. DOI PubMed
14. Choi S, Jung M, Jeong M, et al. Postmortem changes in mRNA expression and tissue morphology in brain and femoral muscle tissues of rat. *Int J Mol Sci.* 2025;26:7059. DOI PubMed PMC
15. Raekallio J. On the enzyme-histochemical vital reactions of skin wounds. *Dtsch Z Gesamte Gerichtl Med.* 1967;59:54-63. PubMed
16. Wang L, Zhao R, Liu C, et al. A fundamental study on the dynamics of multiple biomarkers in mouse excisional wounds for wound age estimation. *J Forensic Leg Med.* 2016;39:138-46. DOI
17. Kondo T, Ohshima T. The dynamics of inflammatory cytokines in the healing process of mouse skin wound: a preliminary study for possible wound age determination. *Int J Legal Med.* 1996;108:231-6. DOI
18. Li N, Du Q, Bai R, Sun J. Vitality and wound-age estimation in forensic pathology: review and future prospects. *Forensics Sci Res.* 2018;5:15-24. DOI PubMed PMC
19. Kim H, Lee Y, Kim VN. The biogenesis and regulation of animal microRNAs. *Nat Rev Mol Cell Biol.* 2024;26:276-96. DOI
20. Bartel DP. MicroRNAs: Target recognition and regulatory functions. *Cell.* 2009;136:215-33. DOI PubMed PMC
21. Lu TX, Rothenberg ME. MicroRNA. *J Allergy Clin Immunol.* 2018;141:1202-7. DOI PubMed PMC
22. Meng S, Wei Q, Chen S, et al. MiR-141-3p-functionalized exosomes loaded in dissolvable microneedle arrays for hypertrophic scar treatment. *Small.* 2023;20:2305374. DOI PubMed
23. Wei Q, Su J, Meng S, et al. MiR-17-5p-engineered sEVs encapsulated in GelMA hydrogel facilitated diabetic wound healing by targeting PTEN and p21. *Adv Sci.* 2024;11:2307761. DOI PubMed PMC
24. Siu MC, Voisey J, Zang T, Cuttle L. MicroRNAs involved in human skin burns, wound healing and scarring. *Wound Repair Regen.* 2023;31:439-53. DOI
25. Suo L, Cheng J, Yuan H, et al. miR-26a/30d/152 are reliable reference genes for miRNA quantification in skin wound age estimation. *Forensics Sci Res.* 2023;8:230-40. DOI PubMed PMC
26. Ohshima T. Forensic wound examination. *Forensic Sci Int.* 2000;113:153-64. DOI PubMed
27. Kondo T. Timing of skin wounds. *Leg Med.* 2007;9:109-14. DOI PubMed
28. Wei G, Sun L, Li R, Li L, Xu J, Ma F. Dynamic miRNA-mRNA regulations are essential for maintaining Drosophila immune homeostasis during Micrococcus luteus infection. *Dev Comp Immunol.* 2018;81:210-24. DOI
29. Li H, Lin L, Chong L, et al. Time-resolved mRNA and miRNA expression profiling reveals crucial coregulation of molecular pathways involved in epithelial–pneumococcal interactions. *Immunol Cell Biol.* 2020;98:726-42. DOI PubMed PMC
30. Dong Y, Zhang N, Zhao S, Chen X, Li F, Tao X. miR-221-3p and miR-15b-5p promote cell proliferation and invasion by targeting Axin2 in liver cancer. *Oncol Lett.* 2019. DOI PubMed PMC
31. Li Y, Zhang J, Shi J, et al. Exosomes derived from human adipose mesenchymal stem cells attenuate hypertrophic scar fibrosis by miR-192-5p/IL-17RA/Smad axis. *Stem Cell Res Ther.* 2021;12:221. DOI PubMed PMC
32. Dong J, Huth WJ, Marcel N, Zhang Z, Lin L, Lu L. miR-15/16 clusters restrict effector Treg cell differentiation and function. *J Exp Med.* 2023;220:e20230321. DOI PubMed PMC
33. Chen S, Ye J, Lin Y, et al. Crucial Roles of RSAD2/viperin in immunomodulation, mitochondrial metabolism and autoimmune diseases. *Inflammation.* 2024;48:520-40. DOI
34. Zhang W, Zhang D, Wang X, et al. Activation of the RSAD2-YTHDF1 axis in smooth muscle causes inflammatory bowel disease via intercellular mitochondrial transfer. *Nat Commun.* 2025;17:976. DOI PubMed PMC
35. Ding X, Zhou Y, Qiu X, et al. RSAD2: A pathogenic interferon-stimulated gene at the maternal-fetal interface of patients with systemic lupus erythematosus. *Cell Reports Medicine.* 2025;6:101974. DOI PubMed PMC
36. Rivera-serrano EE, Gizzi AS, Arnold JJ, Grove TL, Almo SC, Cameron CE. Viperin reveals its true function. *Annu. Rev. Virol.* 2020;7:421-46. DOI PubMed PMC
37. Wang X, Zhang Y, Jiang B, et al. Study on the role of Hsa-miR-31-5p in hypertrophic scar formation and the mechanism. *Exp Cell Res.* 2017;361:201-9. DOI

38. Zeeuwen P, Van Vlijmen-Willems I, Egami H, Schalkwijk J. Cystatin M/E expression in inflammatory and neoplastic skin disorders. *Br J Dermatol.* 2002;147:87-94. DOI PubMed

39. Zeeuwen PL, Cheng T, Schalkwijk J. The biology of cystatin M/E and its cognate target proteases. *J Investig Dermatol.* 2009;129:1327-38. DOI PubMed

40. Qin C, Zhao B, Wang Y, et al. Extracellular vesicles miR-31-5p promotes pancreatic cancer chemoresistance via regulating LATS2-Hippo pathway and promoting SPARC secretion from pancreatic stellate cells. *J of Extracellular Vesicle.* 2024;13:e12488. DOI PubMed PMC

41. Van Den Bogaard EH, Van Geel M, Van Vlijmen-Willems IM, et al. Deficiency of the human cysteine protease inhibitor cystatin M/E causes hypotrichosis and dry skin. *Genet Med.* 2019;21:1559-67. DOI PubMed PMC